

Anisotropic drop morphologies on corrugated surfaces

H. Kusumaatmaja*, R. J. Vrancken[†], C.W.M. Bastiaansen[†], and J. M. Yeomans*

*The Rudolf Peierls Centre for Theoretical Physics, Oxford University,
1 Keble Road, Oxford OX1 3NP, U.K. and

[†]Chemical Engineering and Chemistry Department,
Eindhoven University of Technology, Eindhoven 5600 MB, The Netherlands

February 10, 2022

Abstract

The spreading of liquid drops on surfaces corrugated with micron-scale parallel grooves is studied both experimentally and numerically. Because of the surface patterning, the typical final drop shape is no longer spherical. The elongation direction can be either parallel or perpendicular to the direction of the grooves, depending on the initial drop conditions. We interpret this result as a consequence of both the anisotropy of the contact line movement over the surface and the difference in the motion of the advancing and receding contact lines. Parallel to the grooves, we find little hysteresis due to the surface patterning and that the average contact angle approximately conforms to Wenzel's law as long as the drop radius is much larger than the typical length scale of the grooves. Perpendicular to the grooves, the contact line can be pinned at the edges of the ridges leading to large contact angle hysteresis.

1 Introduction

In recent years wetting and spreading phenomena have received continued attention from the scientific community due to their broad application in, for example, microfluidic devices, surface coating and biomimetics. Surface roughness can be exploited to significantly alter the behaviour of fluids moving over a surface. Examples include plants where micron-scale bumps on the leaves lead to superhydrophobic behaviour [1], desert beetles who use hydrophilic patches on their back to collect dew [2], and butterfly wings which are patterned anisotropically to promote directional run-off [3].

It is now possible to reproduce heterogeneous surface patterning in a very controlled manner on micron length scales. Regular arrays of chemical patches [4, 5, 6] and posts [7, 8, 9, 10]

of different shapes and sizes are regularly fabricated and several authors [11, 12, 13] have even shown the possibilities of manufacturing multi-scale surface patterns. Recently such patterning has been used to control the movement of drops [16, 17] and to attempt to enhance flow in microchannels [18, 19].

The motion of drops on patterned surfaces is complex because of pinning and hysteresis. In particular surfaces with anisotropic patterning on a scale comparable to the drop size can result in elongated drop shapes and in a different motion parallel and perpendicular to the grooves. Gleiche *et al.* [4] showed that there is an anisotropy in the average value of contact angle and contact angle hysteresis on chemically nanostructured surfaces. Brandon *et al.* [20] investigated the effect of drop size on chemically striped surfaces and found that the drop anisotropy and contact angle hysteresis depended on the drop volume. Elongated drop shapes were also obtained by Chen *et al.* [21] and Chung *et al.* [22] for hydrophobic and hydrophilic grooved surfaces respectively. Narhe and Beysens [23] studied the growth dynamics of water drops condensing on grooved surfaces and showed that similar elongated drop shapes can be found during growth when the surface is hydrophilic, but is absent when the surface is superhydrophobic. Pakkanen and Hirvi [24] further showed that the anisotropy still persists when surface patterning is nanoscopic. Morita *et al.* [5] and Yoshimitsu *et al.* [10] studied the dynamics of drops sliding on chemically striped and hydrophobic grooved surfaces and found that the sliding angles are considerably larger for drops moving perpendicular to the stripes.

In this paper we present a number of experiments and lattice Boltzmann simulations of drops spreading or dewetting on a hydrophilic surface patterned with parallel grooves. Our results highlight the importance of hysteresis and energetic barriers due to the surface patterning: because of the asymmetric behaviour of the advancing and receding contact line, the final drop shape can be elongated either along or perpendicular to the grooves. When the contact line is advancing, the drop is found to be elongated parallel to the grooves. On the other hand, when the contact line is receding, the drop is elongated perpendicular to the grooves. We present both equilibrium and quasi-static drop experiments and simulations in section 4. In section 5, an investigation of the influence of three dimensionless surface parameters is presented: the roughness factor, the aspect ratio of the barriers and the dimensions of the drop versus the dimensions of the barriers. As expected, the contact angle, particularly that of the interface lying perpendicular to the grooves, strongly depends on both the parameters of the surface and the history of the drop motion. The complementary nature of experiments and simulations is also demonstrated. Sections 2 and 3 summarise the experimental and numerical approaches respectively.

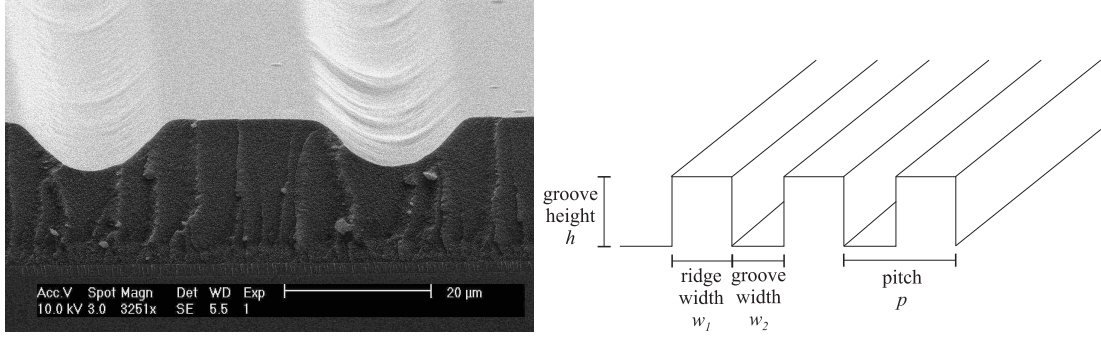


Figure 1: Periodically corrugated surfaces used in the (a) experiments and (b) simulations.

2 Experiments

Two sets of experiments were performed with anisotropically grooved surfaces.

In the first set of experiments, micron-sized droplets were placed on sub micron-scale corrugated polyimide surfaces. The polyimide layers were created on glass by spincoating a commercially available mixture (JSR AL-3046) of polyimide from solvent. After spincoating, the samples were heated for 5 minutes at 80°C on a hotplate to evaporate the solvent, and afterwards thermally cured in a vacuum oven at 180°C for 1.5 hours. Afterwards the samples were rubbed unidirectionally with a velvet cloth with a force $\sim 1 \text{ kg/cm}^2$ over a distance of 30 cm with a velocity of 10 cm/s. This created grooves that were determined by AFM to be between 15 to 20 nm deep and 50 to 200 nm wide. Non-rubbed surfaces were prepared identically, only the rubbing step was omitted.

Surface energy measurements were made on the prepared polyimide surfaces. By measuring the contact angle of water, ethylene glycol and diiodomethane drops on the surface, the surface energy was calculated to be 43.6 mN/m, employing the OWRK method.

Drops consisting of a monomer of 99.0 w% ethoxylated bisphenol-A dimethacrylate (Sartomer Europe BV), having a surface tension of 41 mN/m, together with 1.0 w% photo-initiator (Irgacure 184, Ciba Specialty Chemicals), were placed on the surface by two methods. In the first method, the mixture was sprayed manually onto the polyimide surface. The resulting drops were placed randomly on the surface and were of varying size. In the second method, micro-transfer printing [14], a PDMS elastomeric stamp with an array of trapezoidal posts with face areas of $100 \times 100 \text{ μm}$ was pressed into a thin spincoated layer of monomer mixture and afterwards pressed against the polyimide layer. Part of the mixture was transferred to the polyimide surface, after which the stamp was detached from the surface leaving an array of drops with equal size. The drops were polymerized within one minute after placement. This fixed the geometry of the drop and enabled analysis afterwards, while still allowing the drop sufficient time to equilibrate. The drop $x - y - z$ profiles were determined by optical interferometry (Fogale Zoomsurf 3D), and the parallel and perpendicular cross-sectional height

profiles were extracted and ellipse-fitted to determine the contact angles and elongation. A minimum of five drops were examined for each surface.

In the second set of experiments, smooth corrugated polymer surfaces were created by means of a four-step process called photo-embossing [15]. First a so-called photo-polymer layer was spin-coated on glass forming layers approximately 20 μm thick. The mixture consisted of 41.9 w% monomer dipentaerythritol penta/hexa-acrylate (Sigma Aldrich), 41.9 w% polymer polybenzylmethacrylate (Mw 70 kg/mol; Scientific Polymer Products), 4.20 w% photo-initiator Irgacure 819 (Ciba Specialty Chemicals) and 12.0 w% inhibitor tert-butyl hydroquinone (Aldrich). In the second step, the layer was illuminated with UV light through a suitable lithographic mask (described below), partially polymerizing the exposed parts of the layer. In the third step, the sample was heated and part of the monomers in the non-illuminated regions diffused towards the illuminated regions, creating the corrugated surface. In the last step the surface was flood-exposed with UV light to polymerize the full layer. Similarly to the polyimide surface, the photo-embossed surface was found to have a surface energy of 44.7 mN/m.

The lithographic masks employed had sizes of 1 x 1 cm and consisted of parallel stripes, where each stripe was as wide as the distance between the stripes, i.e. 50 % of the incident light is transmitted. The pitch, i.e. the repeat length of the mask (line to line) was varied from 10 μm to 100 μm . The depth of the grooves could be varied between 100 nm and 5 μm by varying the illumination time, with the exception that the maximum depth could only be reached with masks with pitches above 40 μm because sufficient material needs to be available to be displaced by the photo-embossing process. The depth of the grooves was again determined with optical interferometry.

Water drops of 4 μl were placed on the photo-embossed polymer surfaces by an automated dispensing needle (Optical Contact Angle setup, Dataphysics) at a constant height above the surface to minimize any variations in drop placement. The water used for the measurements was purified (Millipore Super-Q) and CO_2 was removed (Elix-10 UV). The drop properties were measured on the surface with the contact angle measurement setup. Both θ_{\parallel} and θ_{\perp} were determined, as well as the drop elongation e . The contact angles and base radii were determined by means of digital drop shape fitting employing an ellipse fitting algorithm.

The two sets of experiments are complementary, in that they employ different surfaces and probe liquids. The rubbed surfaces have nano-meter scale corrugations, whereas the photo-embossed surfaces have micron-scaled corrugations. Micro-transfer printing is suitable for creating well-defined dewetting drops, while photo-embossed surfaces have the great benefit of being smooth as well as controllable with regards to the size of the corrugations. In the following sections the results from both sets of experiments are presented next to each other highlighting different aspects of anisotropic hysteresis.

3 Lattice Boltzmann simulations

We use a mesoscale simulation approach where the equilibrium properties of the drop are modelled by a continuum free energy

$$\Psi = \int_V (\psi_b(n) + \frac{\kappa}{2}(\partial_\alpha n)^2) dV + \int_S \psi_s(n_s) dS. \quad (1)$$

$\psi_b(n)$ is a bulk free energy term which we take to be [26]

$$\psi_b(n) = p_c(\nu_n + 1)^2(\nu_n^2 - 2\nu_n + 3 - 2\beta\tau_w), \quad (2)$$

where $\nu_n = (n - n_c)/n_c$, $\tau_w = (T_c - T)/T_c$ and n , n_c , T , T_c and p_c are the local density, critical density, local temperature, critical temperature and critical pressure of the fluid respectively. This choice of free energy leads to two coexisting bulk phases (liquid and gas) of density $n_c(1 \pm \sqrt{\beta\tau_w})$. The second term in Eq. (1) models the free energy associated with any interfaces in the system. κ is related to the surface tension via $\gamma = (4\sqrt{2\kappa p_c}(\beta\tau_w)^{3/2}n_c)/3$ [26]. The last term in Eq. (1) describes the interactions between the fluid and the solid surface. Following Cahn [27] the surface energy density is taken to be $\psi_s(n) = -\phi n_s$, where n_s is the value of the fluid density at the surface. The strength of interaction, and hence the local equilibrium contact angle, θ_e , is parameterized by the variable ϕ . Here the simulation parameters are chosen to give $n_{\text{liquid}} = 4.11$, $n_{\text{gas}} = 2.89$, $\gamma = 5.14 \times 10^{-4}$, and $\theta_e = 70^\circ$. The typical drop and pattern sizes are of order 100 and 10 lattice spacings respectively. Simulation and physical parameters are related by choosing a length scale l_0 , a time scale t_0 , and a mass scale m_0 . A simulation parameter with dimensions $[l]^{n_1}[t]^{n_2}[m]^{n_3}$ is multiplied by $[l_0]^{n_1}[t_0]^{n_2}[m_0]^{n_3}$ to give the physical value [28]. More specific details on the model used here, including the way we have implemented complicated surface geometries, can be found in [29].

The dynamics of the drop is described by the continuity (3) and the Navier-Stokes equations (4)

$$\partial_t n + \partial_\alpha (n u_\alpha) = 0, \quad (3)$$

$$\partial_t (n u_\alpha) + \partial_\beta (n u_\alpha u_\beta) = -\partial_\beta P_{\alpha\beta} + \nu \partial_\beta [n(\partial_\beta u_\alpha + \partial_\alpha u_\beta + \delta_{\alpha\beta} \partial_\gamma u_\gamma)], \quad (4)$$

where \mathbf{u} , \mathbf{P} , and ν are the local velocity, pressure tensor, and kinematic viscosity respectively. The thermodynamic properties of the drop are input via the pressure tensor \mathbf{P} which is calculated from the free energy [26, 29, 28] via

$$P_{\alpha\beta} = (p_b(n) - \frac{\kappa}{2}(\partial_\alpha n)^2 - \kappa n \partial_\gamma \gamma n) \delta_{\alpha\beta} + \kappa (\partial_\alpha n)(\partial_\beta n), \quad (5)$$

$$p_b(n) = p_c(\nu_n + 1)^2(3\nu_n^2 - 2\nu_n + 1 - 2\beta\tau_w). \quad (6)$$

Eqs. (3) and (4) are solved using a lattice Boltzmann algorithm [26, 29, 28, 30, 31].

This model (or very similar approaches e.g. [32, 33, 34]) has been shown to be a useful tool to study several aspects of drop dynamics on patterned surfaces, such as the problem of contact angle hysteresis [35], and drops spreading on superhydrophobic [29] and chemically patterned surfaces [28].

To render the simulation feasible, the typical surface pattern used in the simulations is slightly different to that produced experimentally. It is therefore important to note here that our aim in this paper is to obtain a consistent qualitative understanding of the problem rather than to attempt to exactly match experiments and simulations. The shape of the grooves is taken to be rectangular, as shown in Fig. 1(b). We define the aspect ratio as the ratio of the groove height to the pitch. No-slip boundary conditions are imposed on the velocity field on the surfaces adjacent to and opposite to the drop and periodic boundary conditions are used in the other two directions.

4 Anisotropic drop morphology on a corrugated surface

In this section, the anisotropy in the final shape of a drop spreading on a corrugated surface is investigated. First, we performed experiments where liquid drops are sprayed or micro-transfer printed onto the rubbed polyimide surface. We find that even though both preparation methods result in an elongated drop shape, the direction of elongation relative to the surface grooves is different. The drop is elongated parallel to the grooves if sprayed, while micro-transfer printed drops are elongated perpendicular to the grooves.

Results consistent with the first set of experiments above were found when water is quasi-statically added to a spreading drop prepared on a photo-embossed surface. Here different qualitative behaviours are observed parallel and perpendicular to the grooves, further highlighting the asymmetry of contact line motion in these two directions. The experiments are then complemented by performing lattice Boltzmann simulations to further understand the role of the surface anisotropy in determining the final shape of the drop.

4.1 Experiments

In Fig. 2(b) we show a typical final shape of a liquid drop that is sprayed onto the surface, causing the the drop contact line to advance to wet the corrugated surface. Since the surface patterning is not isotropic, the advancing contact line behaves differently parallel and perpendicular to the grooves. Based on Johnson and Dettre's work [36] no hysteresis due to the surface patterning is expected in the parallel direction as there are no energetic barriers present which could tend to pin the contact line. On the other hand, perpendicular to the grooves, surface undulations are known to pin the contact line [37, 38, 39]. Contact line

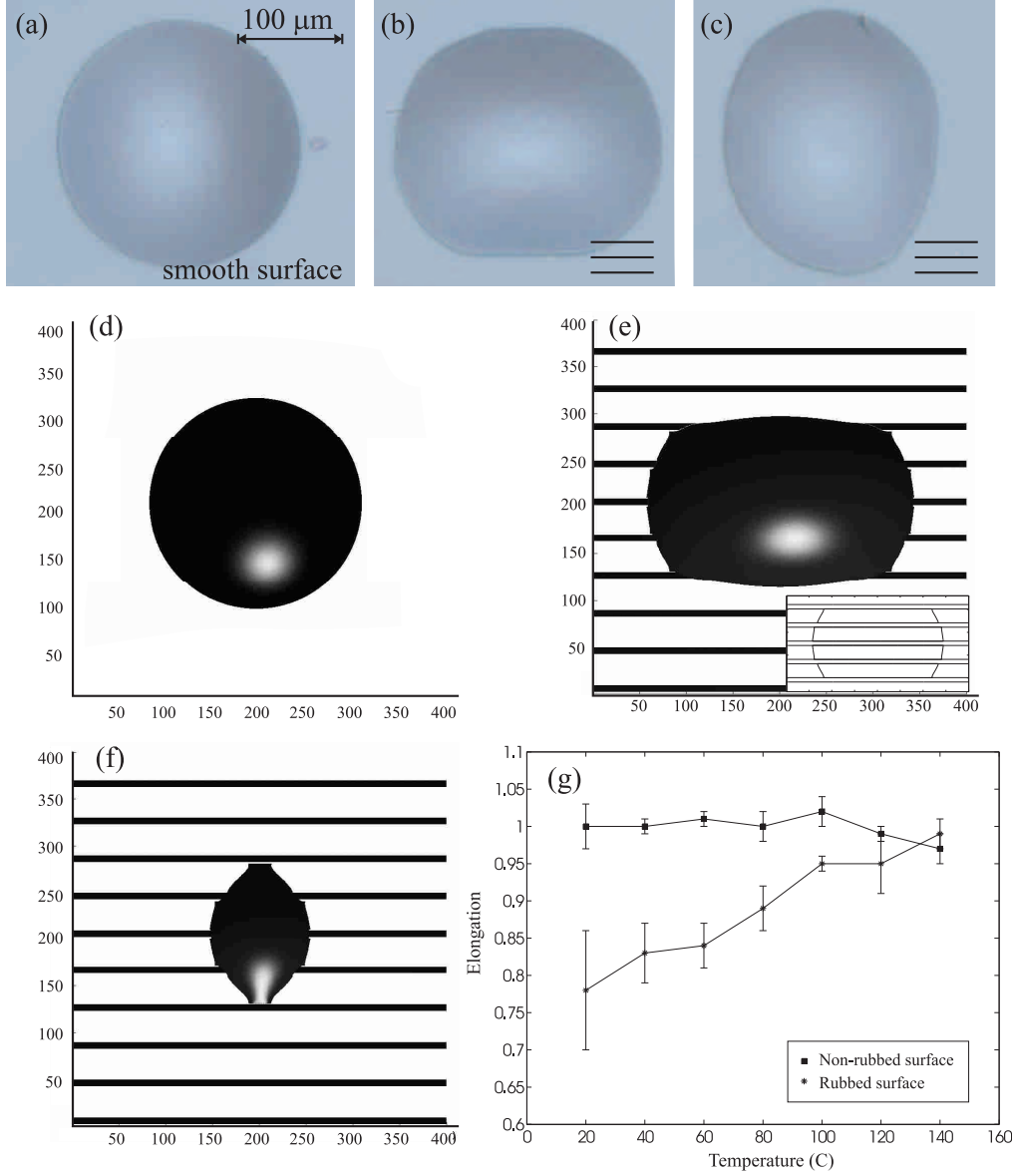


Figure 2: Typical drop shape observed in experiments when (a) there is no surface patterning, (b) the drop is sprayed onto the surface and spreads, and (c) the drop is stamped onto the surface and dewets. Although not visible in this image, the surfaces of (b) and (c) were patterned with sub micron-scale ridges. Here the ridges are oriented in the horizontal direction. (d), (e) and (f) Lattice Boltzmann simulation results when (d) the drop spreads on a smooth surface, (e) and (f) the drop volume is quasi-statically (e) increased and (f) decreased. The experimental drop elongation parallel (b, e) and perpendicular (c, f) to the grooves is clearly reproduced in the simulations. (g) Experimental measurements of the average elongation as function of printing temperature for the printed acrylate drops on rubbed and non-rubbed polyimide. The drops on non-rubbed surfaces have approximately spherical contact lines at all temperatures, whereas with decreasing temperatures the drops on rubbed surfaces become more and more elongated.

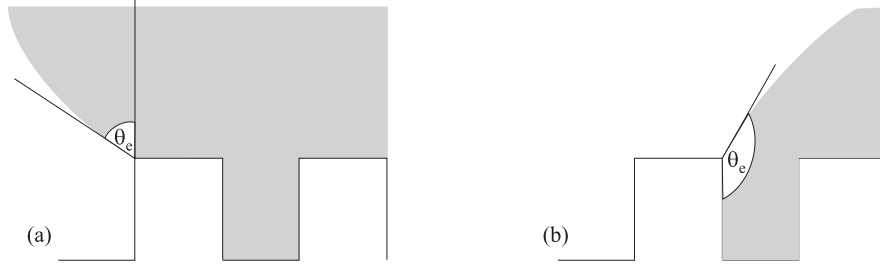


Figure 3: Graphical illustration of Gibbs criteria: (a) advancing and (b) receding contact line.

pinning leads to strong contact angle hysteresis and this causes the advancing contact angle, θ_A , to differ from that in the parallel direction.

The pinning is illustrated in Fig. 3(a). For the drop contact line to advance, it has to wet the side of the grooves, which, according to the Gibbs' criterion [38, 39], occurs when $\theta_A = \theta_e + 90^\circ$ for rectangular ridges. More generally $\theta_A = \theta_e + \alpha$ in two dimensions where α is the maximum inclination of the surface. In three dimensions, the value of the advancing (and receding - see below) angle is not extreme as that predicted by the Gibbs' criteria, due to the energy costs associated with the surface deformation from the spherical cap shape. The advancing angle is, nonetheless, generally larger than the advancing angle parallel to the grooves. As a consequence, it is easier for the drop to spread in the parallel direction and hence the drop shape is elongated parallel to the grooves as shown in Fig. 2(b). This is the final drop shape typically found in corrugated surface experiments [21, 24, 22]. The shape of a drop on a smooth surface is also shown in Fig. 2(a) for comparison.

When the drop is (micro-transfer) printed onto the surface, on the other hand, the drop contact line retreats to dewet the surface, as the liquid is initially spread out much further than its equilibrium shape. This occurs when the drop contact angle is smaller than or equal to the receding contact angle. If no contact angle hysteresis is present, the final drop shape will be independent of the initial conditions. However, as discussed above, hysteresis is an important effect in the perpendicular direction and as a result, the receding angles are again different parallel and perpendicular to the grooves. Contact line pinning for the receding motion is illustrated in Fig. 3(b). For the contact line to recede, the drop has to dewet the side of the posts, which happens when $\theta_R = \theta_e - 90^\circ$ for rectangular ridges. For other geometries, $\theta_R = \theta_e - \alpha$ in two dimensions where α is the maximum inclination of the surface. Since the receding angle in the perpendicular direction is smaller than the receding angle parallel to the grooves, it is easier for the drop to dewet in the parallel direction and the final drop shape is typically elongated perpendicular to the grooves, as shown in Fig. 2(c).

The effect of the printing temperature on the final shape of the printed drops showed an interesting result, as shown in Fig. 2(g). With increasing temperature, the elongation perpendicular to the barriers decreases. Clearly, the pinning ability of the barriers is decreased

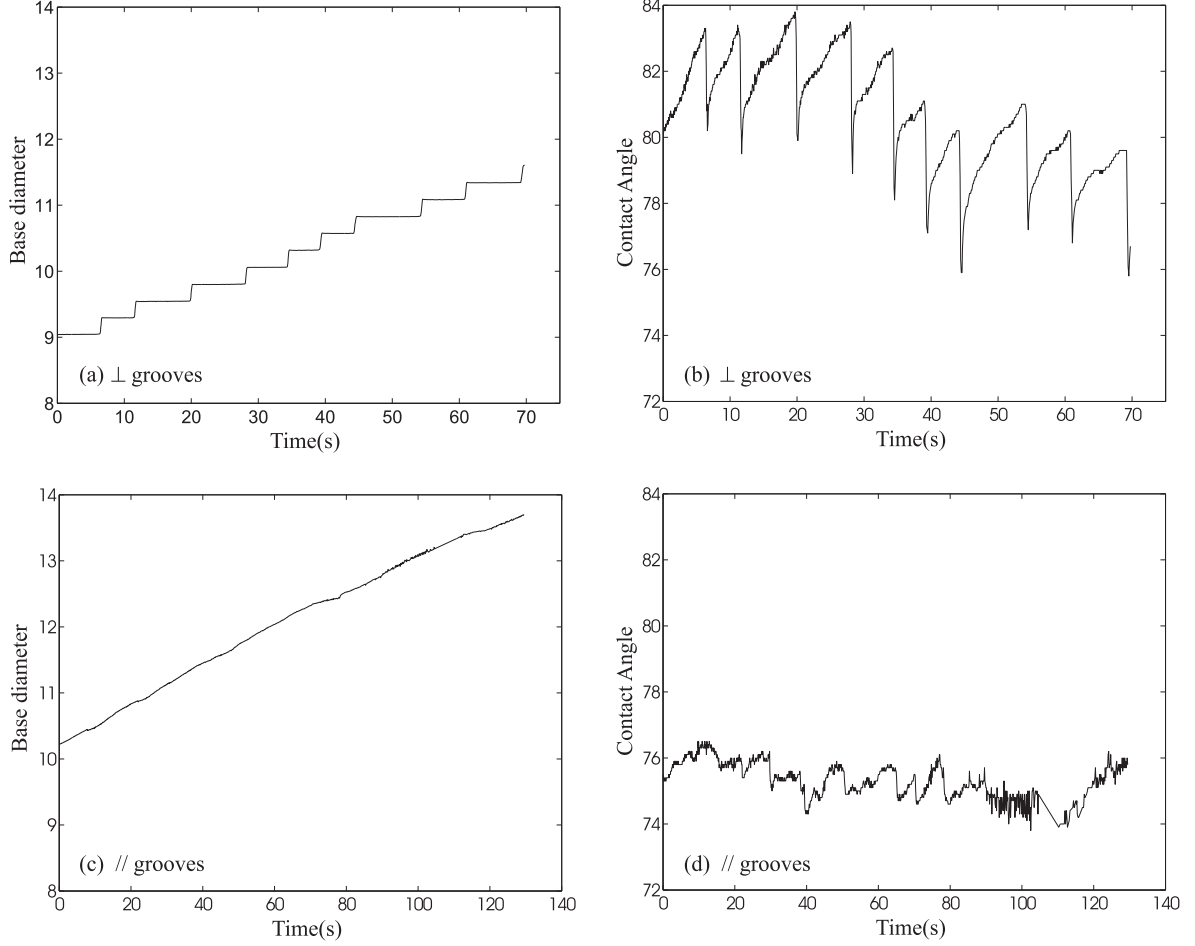


Figure 4: Advancing contact angle measurement for a drop of water spreading on a photo-embossed surface. (a) and (c) are measurements of the base diameter (in arbitrary units because the setup was not length-calibrated), while (b) and (d) are the contact angles as a function of time. (a) and (b) are the diameter and contact angle perpendicular to the grooves, (c) and (d) show the same variables parallel to the grooves. The initial drop volume was $4 \mu\text{l}$. Water was added with $0.06 \mu\text{l}$ per second effecting a quasi-static, linear increase in volume. The surface had a pitch $80 \mu\text{m}$ and groove depth of $4.3 \mu\text{m}$, i.e. an aspect ratio of 0.10. The equilibrium contact angle of the surface was $\theta_e \simeq 70^\circ$. The characteristic effect of crossing surface barriers in the perpendicular direction is clearly visible in (a) and (b), while (c) and (d) demonstrate that in the parallel direction the motion is much smoother.

at higher temperatures and the drop morphology is less affected by hysteresis. A possible explanation for this effect is that the viscosity at higher temperature decreases so that the drop in general and the contact line in particular move faster and dissipate less energy. Even without determining the exact barrier crossing mechanism, in general the interface can more easily overcome pinning on the ridges by having more energy available for deforming its surface locally, enabling it to cross more barriers. This is further supported by our simulation results, where we found similar dependence of drop elongation on the drop viscosity and impact velocity. The typical drop elongation decreased as we reduced the drop viscosity or increased the drop initial kinetic energy.

The mechanism by which the interface crosses the ridges can be envisaged as the nucleation mechanism formulated by DeGennes [25]: in this process an advancing drop will first form a nucleus in the next grooves, after which the interface spreads along the grooves until a new and stable, but less elongated morphology is reached. For drops retracting over the barrier, the inverse process occurs. The drop retreats parallel to the grooves until it becomes sufficiently distorted that it is favourable for it to retract, dewetting the outermost grooves. We were able to observe this retracting mechanism with evaporating water drops which were placed on a photo-embossed surface. This is shown in Fig. 5.

Our interpretation of the role of contact line pinning in determining the drop shape is backed up by the experimental evidence obtained when considering a quasi-statically growing drop on a photo-embossed surface, shown in Figs. 4. The drop contact angles and base radii both parallel and perpendicular to the grooves are measured as a function of drop volume. Three distinct features are visible: (i) the saw-tooth shaped variation with time of the perpendicular contact angle, (ii) the step-shaped variation of the perpendicular base radius and (iii) the absence of these distinct features in the parallel direction where the base radius increases continuously and the contact angle is roughly constant over the whole range of the experiment. Features (i) and (ii) are clear indications of contact line pinning in the perpendicular direction, while feature (iii) shows that pinning of the contact line due to the surface patterning does not occur in the parallel direction, leading to a significantly lower advancing contact angle. These features were reproduced for all aspect ratios and surfaces. For receding contact line, no depinning was observed in the parallel direction, while depinning in the perpendicular direction occurred irregularly, with interfaces sometimes crossing multiple ridges at once. For this reason, reproducibly quantifying the depinning as function of the surface parameters was unsuccessful. We found that, on the unpatterned surfaces, receding contact angle measurements give values of about 15° to 25° with occasional outliers of up to 50° . On the patterned surfaces, receding contact angle measurements in the parallel direction give similar values to those for the unpatterned samples, while the receding angles in the perpendicular direction are on average about 5° lower than those in the parallel direction. The high experimental scatter is attributed to the common problem of measuring very low receding contact angles,

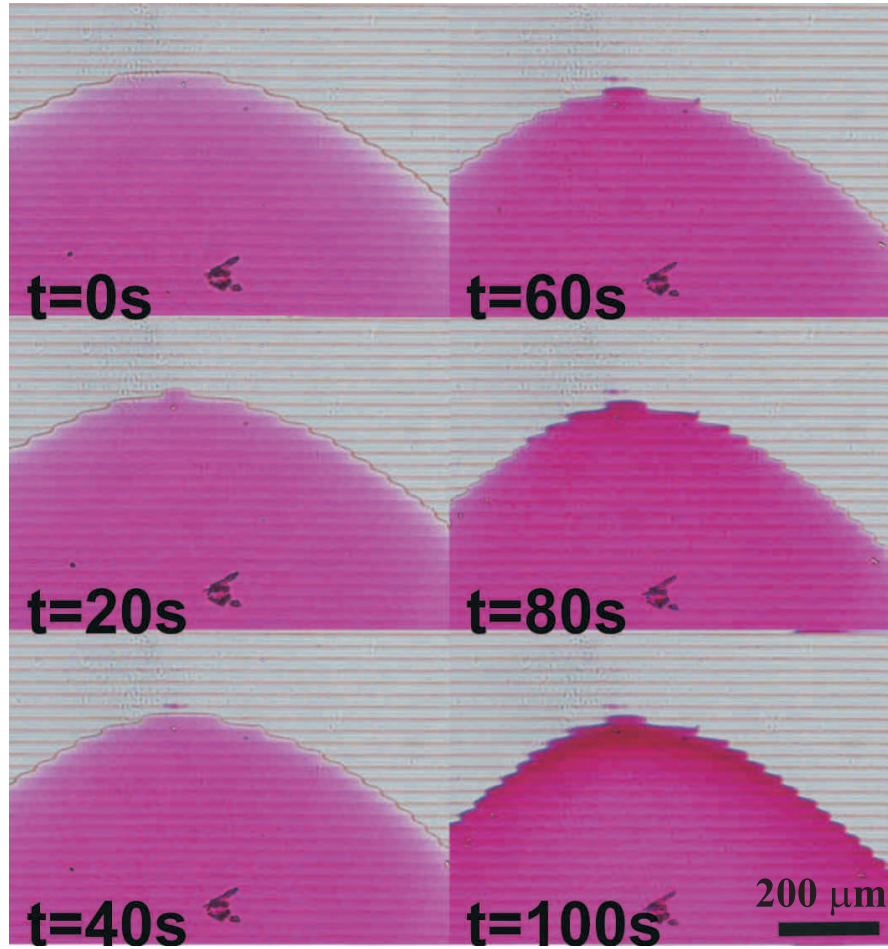


Figure 5: (color online) Microscope observation of the shape of the receding contact line as a water drop evaporates over time. The drop retreats parallel to the grooves until it becomes sufficiently distorted that it is favourable for it to retract, dewetting the outermost grooves. 1% Rhodamine B is added to the drop for visibility.

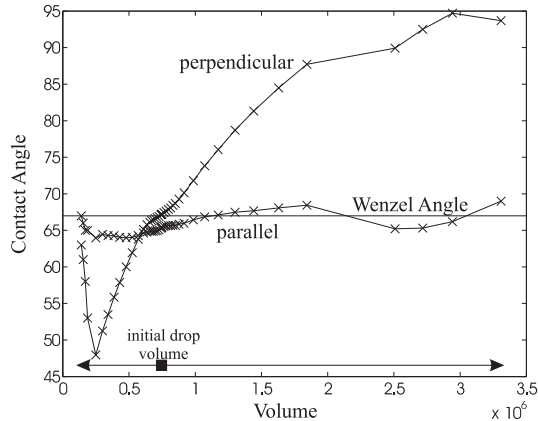


Figure 6: Simulations of drop contact angles on a grooved surface as a function of the drop volume for groove height $h = 3$, ridge width $w_1 = 10$ and pitch $p = 40$. The drop was initialized at $V \sim 0.75 \times 10^6$ and equilibrated. Then the drop volume was either slowly decreased or increased.

namely that incidental pinning and depinning are observed even on (apparently) smooth surfaces. The base radii were also greater in the perpendicular direction, further proving that hysteresis is increased by the barriers.

4.2 Simulations

Similar hysteresis in the motion of the drop perpendicular to the grooves is seen in lattice Boltzmann simulations. A liquid drop was allowed to equilibrate on the corrugated surface. Then, using this as an initial condition, we ran two sets of simulations where the drop volume was quasi-statically increased in the first set and decreased in the second set. To do this, we varied the liquid density by $\pm 0.1\%$ from its equilibrium bulk density every 10000 time steps. This changed the drop volume as the system relaxed back to its coexisting equilibrium densities.

When the drop volume is increased, the drop contact line advances. Therefore, we expect the first set of simulations to mimic a drop sprayed onto the surface and the final drop shape to be elongated parallel to the grooves. When the drop volume is decreased, to the contrary, the drop contact line recedes. We therefore expect the second set to mimic a drop stamped onto the surface and the drop shape to be elongated perpendicular to the grooves. The simulation results shown in Fig. 2 (d) and (e) clearly show that the drop shape is indeed elongated parallel and perpendicular to the grooves when the contact line is (d) advancing and (e) receding. The drop contact angles were also tracked during the simulation and the results are shown in Fig. 6. The main features indicating contact line pinning in the perpendicular direction are again reproduced: (i) the parallel contact angle stays roughly constant and (ii) a large variation in the perpendicular contact angle measurements is observed. Note, however, that due to numerical limitations, it was only possible to follow the drop as it moved over one

groove so that Fig. 6 shows just one period of the repeating sawtooth pattern obtained in the experiments in 4. In the figure the receding contact line jump in the perpendicular direction occurs at $V \sim 0.3 \times 10^6$.

5 Drops spreading on corrugated surfaces: understanding the contact angle measurements

In this section we attempt to provide a consistent picture of the geometry of a drop spreading on corrugated surfaces over a wide range of surface parameters. In particular, we shed light on the influence of three dimensionless surface parameters: the roughness factor, the aspect ratio of the barriers and the relative ratio of the dimensions of the drop to the dimensions of the barriers. Our conclusions will be drawn from both experiments and lattice Boltzmann simulations.

We have demonstrated that the shape of a drop spreading on a corrugated surface is no longer spherical. The drop is elongated either in the direction parallel or perpendicular to the grooves and the contact angle varies along the contact line. In order to simplify the analysis, we focus only on two principal directions: parallel and perpendicular to the grooves, since the greatest difference in contact angle is expected between these two. We define the apparent contact angle as the contact angle made by fitted ellipses at its intersection with the top of the ridges. It is very important to realize, however, that the apparent angle is often not equal to the local contact angle, in particular where the contact line is distorted locally by the corrugations. We also define the aspect ratio as the ratio of the groove height to the pitch and the drop elongation as the ratio of the maximum base radius in the parallel and perpendicular directions.

5.1 Experiments

Fig. 7(a) and (b) show our experimental results on how the drop elongation and contact angles depend on the aspect ratio. In this set of experiments, we prepared photo-embossed surfaces having different corrugations and liquid drops were placed onto the surfaces with a syringe. We first found that there was no obvious relationship between the final drop geometry and either the groove depth or the groove pitch. However, plotting the data against the aspect ratio of the corrugations, trends could be identified, although the scatter was significant. This is expected given the important role of hysteresis and the existence of multiple local energy minima.

There are four aspects of the data which we wish to comment on:

- (i) On chemically striped surfaces, it has been shown experimentally [4] and theoretically [36] that there is no contact angle hysteresis (at least due to the surface patterning) in the

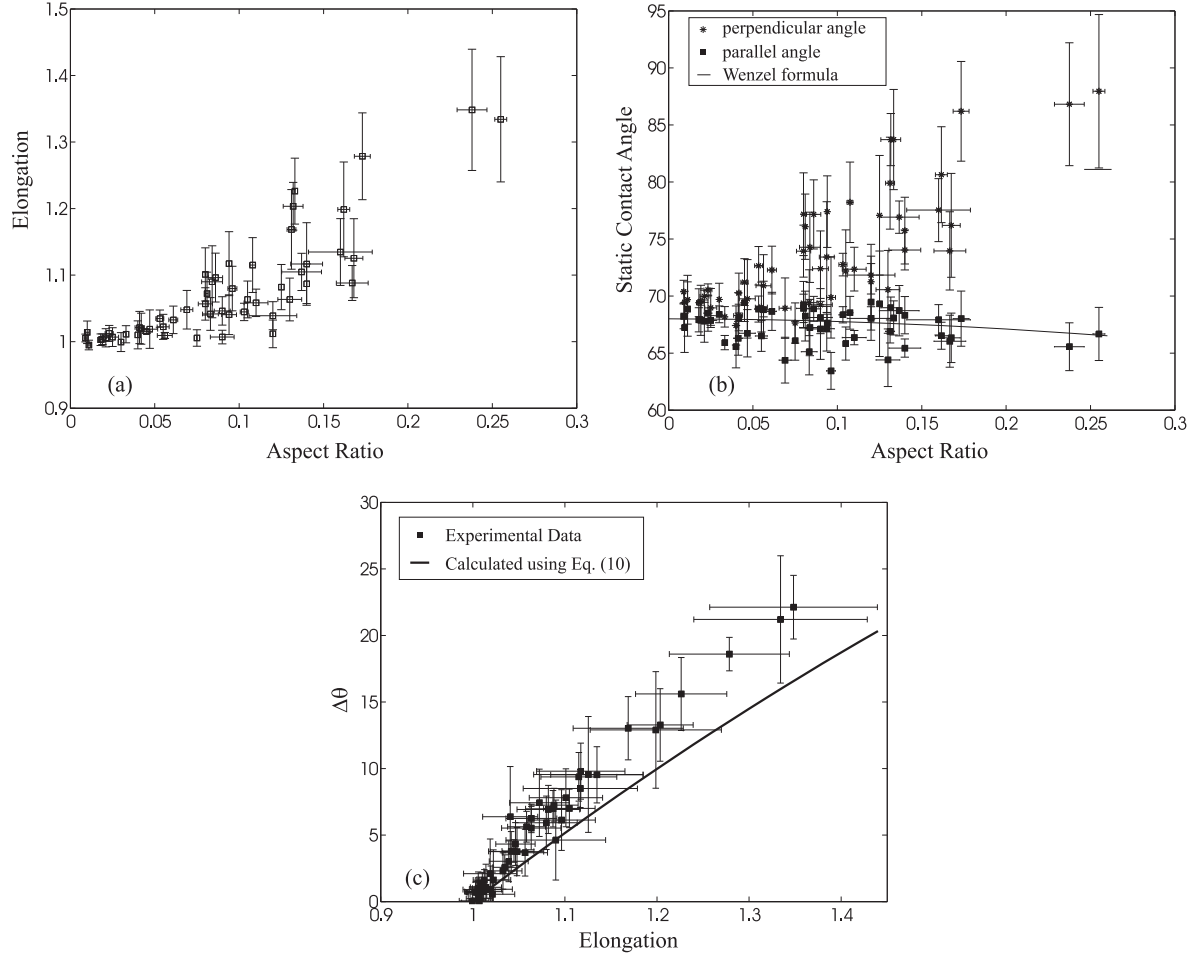


Figure 7: Experimental results for water drops on photo-embossed surfaces. (a) Elongation of the droplet and (b) Static θ_{\parallel} and θ_{\perp} as functions of the aspect ratio of the surface. Both the elongation and θ_{\perp} increase approximately monotonically with increasing aspect ratio. The solid line corresponds to the Wenzel angle. (c) $\Delta\theta = \theta_{\perp} - \theta_{\parallel}$ as a function of elongation. The solid line is the relation between $\Delta\theta$ and the elongation predicted by Eq. 10 and using $\theta_{\parallel} = \theta_{\text{Wenzel}}$.

direction parallel to the stripes. Furthermore, Gleiche *et al.* [4] showed that the parallel contact angle is close to the Cassie-Baxter contact angle [40]. Similarly, in this study, we might expect the parallel angle to approximately follow the Wenzel formula [41],

$$\cos \theta_{\parallel} = r \cos \theta_e, \quad (7)$$

where r is the roughness factor. In the experiments

$$r \simeq \frac{w_1 + \sqrt{w_2^2 + 4h^2}}{p} \quad (8)$$

where $w_1 \simeq w_2$. w_1 , w_2 , h and p are respectively the ridge width, the groove width, the groove height, and the pitch. The equilibrium contact angle $\theta_e \simeq 68^\circ$. In figure 7(b) the Wenzel approximation is indeed shown to correspond well to θ_{\parallel} . The same conclusion was also found in [22].

(ii) The perpendicular contact angle, on the other hand, shows a very large scatter. Typically $\theta_{\perp} > \theta_{\parallel}$, and θ_{\perp} tends to increase with the aspect ratio. This may be explained using the Gibbs' criteria [38] we discussed in the previous section. Since the drop spreads outwards on the corrugated surface, it is appropriate to consider the advancing contact line motion. Therefore, it is easier for the drop to spread parallel to the grooves. This immediately implies that the drop contact angle perpendicular to the grooves is larger than that parallel to the grooves. The maximum value of θ_{\perp} is an estimate of the advancing angle in the perpendicular direction. For the two dimensional model illustrated in Fig. 3, $\theta_A = \theta_e + \alpha$, where α is the maximum slope on the surface. This is clearly an overestimate in three dimensions, since it neglects the energy costs associated with the surface deformation from a spherical cap. Nevertheless, from the data shown in Fig. 7, we found that the advancing angle increases from 70° to 88° with increasing aspect ratio. This is consistent with the fact that, for the experimental substrate geometry, (Fig. 1 (a)), the maximum slope α increases with the aspect ratio of the grooves. Similar behaviour is also observed in Fig. 2(e) of a recent work by Chung *et al.* [22].

(iii) In Fig. 7 (c), we plot the difference between the contact angles $\Delta\theta$ as a function of the drop elongation. We find that $\Delta\theta$ varies monotonically with drop elongation and the experimental scatter is reduced when compared to figure 7 (a) and (b). Qualitatively this can be explained by assuming that the drop shape is close to elliptical. Assume for simplicity that the drop profiles in the two principal directions can be fitted to circles. In this case, the apparent contact angles can be written as

$$\tan \theta_{\parallel}/2 = h/a \quad \text{and} \quad \tan \theta_{\perp}/2 = h/b, \quad (9)$$

where a and b are the drop base lengths in the two principal directions. As a result,

$$\tan \theta_{\perp}/2 = e \tan \theta_{\parallel}/2. \quad (10)$$

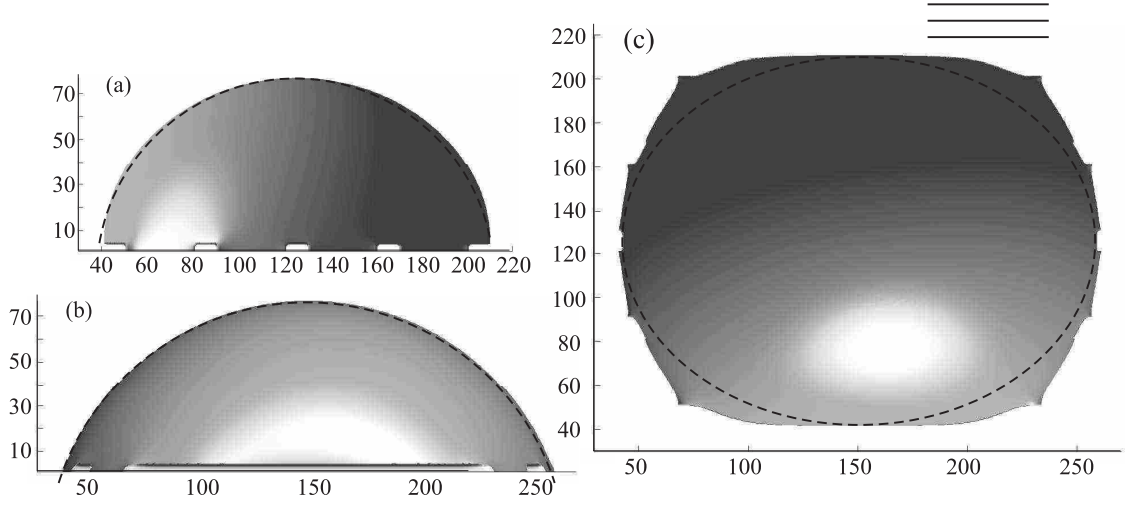


Figure 8: A typical drop shape observed in simulations. (a) and (b) the drop cross sections in the direction parallel and perpendicular to the grooves. (c) Top view of the drop. The dashed lines are fits to (a) and (b) a circle or (c) an ellipse.

θ_{\parallel} is approximately constant in the experiments and hence θ_{\perp} increases monotonically with e . In Fig. 7(c), Eq. (10) is plotted assuming $\theta_{\parallel} = \theta_{\text{Wenzel}}$, and again it corresponds well to the trend observed in the experiments.

(iv) The drop elongation e increases monotonically with the aspect ratio. This result follows from the fact that the energy gain of spreading in the direction parallel to the grooves is higher for higher aspect ratio.

5.2 Simulations

To gain further insight into these relationships between surface and drop geometry, simulations were performed. The drop was initialized as a spherical drop just above the surface and was allowed to spread, without any external force, on the corrugated surface. The drop elongation and contact angles were then recorded after 400000 time steps, by which time the drop had reached its (meta) stable configuration. A typical final drop shape is shown in Fig. 8. As shown in Fig. 8(a) and (b) the drop cross sections in the direction parallel and perpendicular to the grooves can be fitted well with ellipses. We have also tried to fit the contact line around the base of the drop, see e.g. figure 8(c), but the typical fit we obtain is poor: indeed, the top view of the drop clearly shows a corrugated contact line. The corrugation is more noticeable with increasing aspect ratio. This is due to the fact that it is more advantageous to wet the sides of the grooves the higher the aspect ratio. This is similar to changing the wettability ratio between the hydrophilic and hydrophobic stripes on chemically striped surfaces.

The simulation results are presented in Table 1 and Fig. 9. In interpreting the data it is important to note that there were two differences to the experiments forced upon us by

w_1	h	θ_{\perp}	θ_{\parallel}	θ_{Wenzel}	e
10	3	67.19	65.44	66.84	1.034
10	5	65.85	61.70	64.69	1.084
10	8	62.83	57.45	61.39	1.114
10	10	58.82	52.92	59.13	1.133
10	15	43.61	37.41	53.23	1.182

Table 1: Drop contact angles and elongation for different groove heights. The drop volume is $\sim 7.47 \times 10^5$ and the groove width and pitch are kept constant at 30 and 40 respectively. θ_{Wenzel} is the theoretical Wenzel angle. Here the drops only lie on 4 grooves.

computational requirements. Firstly, the dimensions of the simulated drop were comparable to the dimension of the grooves so that a drop lies on only 4 to 5 barriers. Secondly, the ridges were taken to be rectangular so that the maximum slope $\alpha = 90^\circ$ was independent of the aspect ratio. We varied the groove depth but kept the other parameters the same. In the simulations

$$r = 1 + \frac{2h}{p}. \quad (11)$$

Of the experimental features listed in the previous subsection, (iii) $\Delta\theta$ increases with increasing elongation e , and (iv) the drop elongation increases with increasing aspect ratio, are reproduced in the simulations, as shown in Fig. 9(a) and (c). These trends are observed for the same reasons as in the experiments.

The experimental trends (i) and (ii) are, however, not reproduced by the simulations for the following reasons:

(i) $\theta_{\parallel} \simeq \theta_{\text{Wenzel}}$: in the simulations (shown in Fig. 9(b)), the Wenzel angle is a poor approximation for the parallel contact angle, even though both simulations and experiments are in the same aspect ratio regime. The reason for this discrepancy is that the size of the heterogeneities is of the same order as the size of the drop. Since the drop only lies on a small number of grooves, the Wenzel equation is not applicable. For this reason we performed a second set of simulations where the size of the ridges is an order of magnitude smaller than the drop, as shown in Table 2 and Fig. 10, and found the Wenzel equation is indeed a reasonable approximation to the parallel contact angle. In this case, we note that the size of the ridges is comparable to the width of the interface in the lattice Boltzmann simulations and the roughness factor is much higher than that obtained in the experiments. In other words, as long as the typical length scale of the corrugation is much smaller than the drop size, the Wenzel equation is a good estimate of the parallel contact angle.

(ii) $\theta_{\perp} > \theta_{\parallel}$ and θ_{\perp} on average increases with increasing aspect ratio: from Fig. 9(b) we indeed found that $\theta_{\perp} > \theta_{\parallel}$, however, from the data we have so far, increasing the aspect ratio

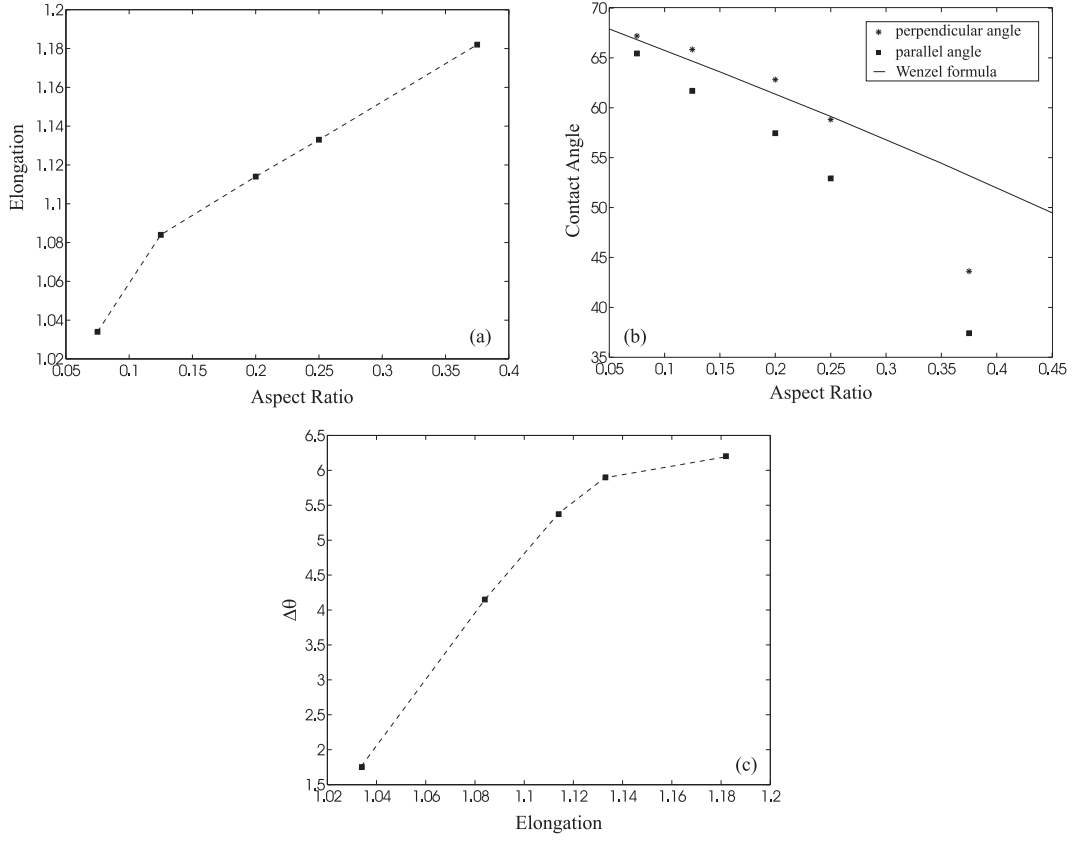


Figure 9: Lattice Boltzmann simulation results for drops on a corrugated surface. (a) Elongation of the droplet and (b) θ_{\parallel} and θ_{\perp} as function of the aspect ratio of the surface. The elongation increases monotonically with increasing aspect ratio, but both θ_{\parallel} and θ_{\perp} decrease. The straight line corresponds to the Wenzel formula. (c) $\Delta\theta$ as a function of the elongation. (The dotted lines in (a) and (c) are guides to the eye.)

w_1	p	θ_{\perp}	θ_{\parallel}	θ_{Wenzel}	e
4	8	57.64	45.42	46.84	1.314
6	10	61.03	51.95	52.00	1.210
8	12	59.30	54.68	55.24	1.101

Table 2: Drop contact angles and elongation for different groove widths. The drop volume is $\sim 7.42 \times 10^5$ and the barrier width and height are kept constant at 4 and 4 respectively. θ_{Wenzel} is the theoretical Wenzel angle.

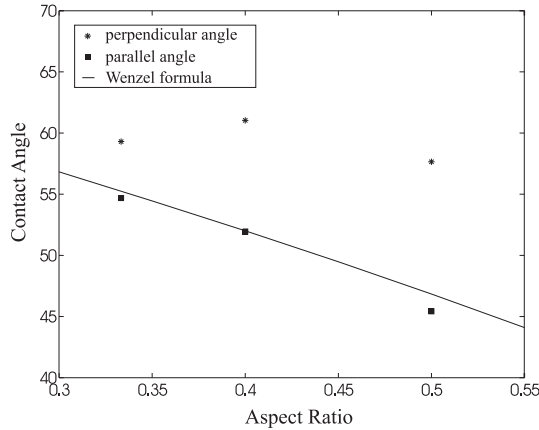


Figure 10: θ_{\parallel} and θ_{\perp} as a function of the aspect ratio of the surface. Here the size of the ridges is much smaller than the size of the drop. The solid line is the theoretical Wenzel angle.

is not followed by an increase in θ_{\perp} ; instead a decrease was found. We now argue why this may be the case. In the experiments, the roughness factor is close to 1 (at most 1.06, from equation 8) and hence θ_{\parallel} is typically just below θ_e . Furthermore, θ_A increases with the aspect ratio since α increases with the aspect ratio. Since $\theta_{\parallel} < \theta_{\perp} < \theta_A$, θ_{\perp} increases with increasing aspect ratio. In the simulations, on the other hand, r is considerably larger than 1 (between 1.15 and 2) and hence θ_{\parallel} is much smaller than θ_e . Since the lower limit of the allowed values of θ_{\perp} is decreased, it is plausible that we find θ_{\perp} decreasing with increasing aspect ratio in Fig. 9(b).

6 Conclusions

We have used experiments and simulations to investigate the behaviour of drops on surfaces patterned with sub-micron and micron-scale parallel grooves. We find that the final drop shape is highly dependent on the path by which it is achieved. Drops which advance across the surface are elongated parallel to the grooves whereas drops that dewet the surface are elongated perpendicular to the grooves. We explain this behaviour in terms of the pinning of the contact line on the groove edges. We stress that it is not possible to measure a single contact angle for a drop on a patterned surface. The contact angle varies around the rim of the drop, with its position on the surface and with its dynamic history.

Contact angles and base dimensions were measured for drops spreading on corrugated surfaces. This was done for a large number of drops and substrate geometries. The data was very noisy, underlining the prevalence of hysteresis on patterned surfaces. However, we were able to draw several conclusions from the results. We find that the parallel contact angle is close to the Wenzel angle. The Wenzel angle in return depends on the roughness factor of the surface. Pinning effects render results for the perpendicular contact angles very noisy but they are,

in general, greater than the parallel angles and tend to increase with increasing aspect ratio. The difference between parallel and perpendicular contact angles increases with the drop elongation whilst the drop elongation increases with the aspect ratio. This behaviour is explained, again by considering contact line pinning, and by noting that the drop spreads more quickly in the parallel direction on surfaces with higher aspect ratio.

We found that lattice Boltzmann simulations of drop motion were of great use in interpreting the experiments. The same relation between the direction of elongation of the drop and its direction of motion over the surface was immediately apparent in the simulations, and we were able to probe the pinning perpendicular to the grooves. Differences in detail between the simulations and experiments arose because the simulations are limited to drops lying on a small number of grooves. In particular, we find that the Wenzel angle no longer provides a good estimate of the parallel angle when the drop dimensions are comparable to the dimensions of the corrugation. An interesting future project would be to perform experiments on wider grooves where a quantitative match to the simulations may be possible.

Acknowledgements

(RV) Ko Hermans for practical help with photo-embossing, Marshall Ming and Paul van der Schoot for useful discussion. (HK) Matthew Blow and Ciro Sempredon for useful discussions. HK acknowledges support from a Clarendon Bursary and the INFLUS project.

References

- [1] Barthlott, W.; Neinhuis, C. *Planta* **1997**, *202*, 1.
- [2] Parker, A. R.; Lawrence, C. R. *Nature* **2001**, *414*, 33.
- [3] Zheng, Y. M.; Gao, X. F.; Jiang, L. *Soft Matter* **2007**, *3*, 178.
- [4] Gleiche, M.; Chi, L.; Gedig, E.; Fuchs, H. *Chem.Phys.Chem.* **2001**, *3*, 187.
- [5] Morita, M.; Koga, T.; Otsuka, H.; Takahara, A. *Langmuir* **2005**, *21*, 911.
- [6] Dupuis, A.; Léopoldès, J.; Yeomans, J. M. *Appl. Phys. Lett.* **2005**, *87*, 024103.
- [7] Öner, D.; McCarthy, T. J. *Langmuir* **2000**, *16*, 7777.
- [8] Bico, J.; Marzolin, C.; Quéré, D. *Europhys. Lett.*, **1999**, *47*, 220.
- [9] Seemann, R.; Brinkmann, M.; Kramer, E. J.; Lange, F. F.; Lipowsky, R. *Proc. Nat. Acad. Sci.* **2005**, *102*, 1848.

- [10] Yoshimitsu, Z.; Nakajima, A.; Watanabe, T.; Hashimoto, K. *Langmuir* **2002**, *18*, 5818.
- [11] Zhu, L.; Xiu, J.; Xu, J.; Tamirisa, P. A.; Hess, D. W.; Wong, C.-P. *Langmuir* **2005**, *21*, 11208.
- [12] Gao, X.; Yao, X.; Jiang, L. *Langmuir* **2007**, *23*, 4886.
- [13] Ming, W.; Wu, D.; Benthem, R. v.; With, G. d. *Nano Lett.* **2005**, *5*, 2298
- [14] Sánchez, C.; Verbakel, F.; Escuti, M. J.; Bastiaansen, C. W. M.; Broer, D. J. *Adv. Mater.* **2008**, *20*, 74.
- [15] Hermans, K.; Wolf, F. K.; Perelaer, J.; Janssen, R. A. J.; Schubert, U. S.; Bastiaansen, C. W. M.; Broer, D. J. *Appl. Phys. Lett.* **2007**, *91*, 174103.
- [16] Kusumaatmaja, H.; Yeomans, J. M. *Langmuir* **2007**, *23*, 956.
- [17] Fidalgo, L. M.; Abell, C.; Huck, W. T. S. *Lab Chip* **2007**, *7*, 984.
- [18] Ou, J.; Rothstein, J. P. *Phys. Fluids* **2005**, *17*, 103606.
- [19] Joseph, P.; Cottin-Bizonne, C.; Benoît, J.-M.; Ybert, C.; Journet, C.; Tabeling, P.; Bocquet, L. *Phys. Rev. Lett.* **2006**, *97*, 156104.
- [20] Brandon, S.; Haimovich, N.; Yeger, E.; Marmur, A. *J. Colloid Interface Sci.* **2003**, *263*, 237.
- [21] Chen, Y.; He, B.; Lee, J.; Patankar, N. A. *J. Colloid Interface Sci.* **2005**, *281*, 458.
- [22] Chung, J. Y.; Youngblood, J. P.; Stafford, C. M. *Soft Matter* **2007**, *3*, 1163.
- [23] Narhe, R. D.; Beysens, D. A. *Phys. Rev. Lett.* **2004**, *93*, 076103.
- [24] Pakkanen, T.; Hirvi, J. *Langmuir* **2007**, *23*, 7724.
- [25] de Gennes, P. G. *Rev. Mod. Phys.* **1985**, *57*, 827.
- [26] Briant, A. J.; Wagner, A. J.; Yeomans, J. M. *Phys. Rev. E* **2004**, *69*, 031602.
- [27] Cahn, J. W. *J. Chem. Phys.* **1977**, *66*, 3667.
- [28] Leopoldes, J.; Dupuis, A.; Bucknall, D. G.; Yeomans, J. M. *Langmuir* **2003**, *19*, 9818.
- [29] Dupuis, A.; Yeomans, J. M. *Langmuir* **2005**, *21*, 2624.
- [30] Swift, M. R.; Orlandini, E.; Osborn, W. R.; Yeomans, J. M. *Phys. Rev. E* **1996**, *54*, 5041.
- [31] Succi, S. *The Lattice Boltzmann Equation, For Fluid Dynamics and Beyond*; OUP: 2001.

- [32] Zhang, J. F.; Kwok, D. Y. *Langmuir* **2006**, *22*, 4998.
- [33] Sbragaglia, M.; Benzi, R.; Biferale, L.; Succi, S.; Toschi, F. *Phys. Rev. Lett.*, **2006**, *97*, 204503.
- [34] Hyväluoma, J.; Koponen, A.; Raiskinmäki, P.; Timonen, J. *Eur. Phys. J. E* **2007**, *23*, 289.
- [35] Kusumaatmaja, H.; Yeomans, J. M. *Langmuir* **2007**, *23*, 6019.
- [36] Johnson, R. E.; Dettre, R. H. *J. Phys. Chem.* **1964**, *68*, 1744.
- [37] Oliver, J. F.; Huh, C.; Mason, S. G. *J. Coll. Interf. Sci.* **1977**, *59*, 568.
- [38] Gibbs, J. W. Scientific Papers 1906, Dover reprint; Dover: New York (1961).
- [39] Shuttleworth, R.; Bailey, G. L. J. *Discuss. Faraday Soc.* **1948**, *3*, 16.
- [40] Cassie, A. B. D.; Baxter, S. *Trans. Faraday Soc.* **1944**, *40*, 546.
- [41] Wenzel, R. N. *Ind. Eng. Chem.* **1936**, *28*, 988.